HHS Public Access

Author manuscript

Nat Struct Mol Biol. Author manuscript; available in PMC 2023 September 27.

Published in final edited form as:

Nat Struct Mol Biol. 2023 September ; 30(9): 1295–1302. doi:10.1038/s41594-023-01061-0.

DELE1 oligomerization promotes integrated stress response activation

Jie Yang[1], **Kelsey R. Baron**[2], **Daniel E. Pride**[1], **Anette Schneemann**[1], **Xiaoyan Guo**[3,4], **Wenqian Chen**[1], **Albert S. Song**[1], **Giovanni Aviles**[3], **Martin Kampmann**[3], **R. Luke Wiseman**[2,✉], **Gabriel C. Lander**[1,✉]

[1]Department of Integrative Structural and Computational Biology, Scripps Research, La Jolla, CA, USA.

[2]Department of Molecular Medicine, Scripps Research, La Jolla, CA, USA.

[3]Institute for Neurodegenerative Diseases and Department of Biochemistry and Biophysics, University of California, San Francisco, CA, USA.

[4]Present address: Department of Genetics and Genome Science, University of Connecticut Health Center, Farmington, CT, USA.

Abstract

Mitochondria are dynamic organelles that continually respond to cellular stress. Recent studies have demonstrated that mitochondrial stress is relayed from mitochondria to the cytosol by the release of a proteolytic fragment of DELE1 that binds to the eIF2α kinase HRI to initiate integrated stress response (ISR) signaling. We report the cryo-electron microscopy structure of the C-terminal cleavage product of human DELE1, which assembles into a high-order oligomer. The oligomer consists of eight DELE1 monomers that assemble with D_4 symmetry via two

✉**Correspondence and requests for materials** should be addressed to R. Luke Wiseman or Gabriel C. Lander. wiseman@scripps.edu; glander@scripps.edu.

Author contributions

J.Y. and G.C.L. conceptualized and led the project. J.Y. created all the constructs, purified the proteins, and performed all cryo-EM structure determination, model building and refinement, and mechanistic interpretation. K.R.B. and R.L.W. designed and performed the ATF4 immunoblotting and ATF4 luciferase assay. D.E.P. assisted in purifying the DELE1 mutant recombinant proteins. A.S. performed the sucrose gradient sedimentation assay. J.Y. and W.C. performed the co-IP assays. A.S.S. assisted in the western blot. X.G., G.A., and M.K. generated the ATF4-FLuc reporter cell line. X.G. performed the full-length DELE1 rescue assay. J.Y. wrote the original draft of the paper. G.C.L. and R.L.W. reviewed and edited the paper. All authors commented on the paper.

Online content

Any methods, additional references, Nature Portfolio reporting summaries, source data, extended data, supplementary information, acknowledgements, peer review information; details of author contributions and competing interests; and statements of data and code availability are available at https://doi.org/10.1038/s41594-023-01061-0.

Competing interests

The authors declare no competing interests.

Additional information

Extended data is available for this paper at https://doi.org/10.1038/s41594-023-01061-0.

Supplementary information The online version contains supplementary material available at https://doi.org/10.1038/s41594-023-01061-0.

Peer review information *Nature Structural & Molecular Biology* thanks the anonymous reviewers for their contribution to the peer review of this work. Primary Handling Editor: Katarzyna Ciazynska, in collaboration with the *Nature Structural & Molecular Biology* team. Peer reviewer reports are available.

sets of hydrophobic inter-subunit interactions. We identified the key residues involved in DELE1 oligomerization, and confirmed their role in stabilizing the octamer in vitro and in cells using mutagenesis. We further show that assembly-impaired DELE1 mutants are compromised in their ability to induce HRI-dependent ISR activation in cell culture models. Together, our findings provide molecular insights into the activity of DELE1 and how it signals to promote ISR activity following mitochondrial insult.

Mitochondria are hubs of bioenergetic processes whose homeostasis must be tightly regulated for cellular function and longevity[1–4]. In response to physiological and pathological insults, mitochondria use molecular signals to initiate nuclear transcription of stress response genes as a means of restoring cellular homeostasis. In mammals, mitochondrial stress is relayed to a central pathway known as the integrated stress response (ISR). Four kinases—HRI, PKR, PERK, and GCN2—serve as specific sensors for detecting distinct forms of cellular stress and convergently phosphorylate a common substrate, eukaryotic initiation factor 2α (eIF2α)[5]. Phosphorylation of eIF2α leads to a global repression of protein production while increasing translation of specific mRNA, such as the transcription factor ATF4. The mitochondrially targeted protein DELE1 is a key signaling factor linking mitochondrial dysfunction to the ISR[6,7]. Mitochondrial stress activates the inner mitochondrial membrane protease OMA1, which promotes cleavage of DELE1, resulting in an accumulation of the DELE1 carboxy-terminal domain (DELE1^{CTD}) in the cytosol, where it activates the HRI kinase. Although its critical role in relaying mitochondrial stress to activate the ISR is well-established[6–8], we lack a molecular description of DELE1, which prevents us from understanding the mechanisms by which DELE1 mediates the activation and subsequent signaling of the ISR.

Results

Cryo-EM structure reveals an oligomeric form of active DELE1^{CTD}

DELE1 is a 56-kDa protein containing a mitochondrial targeting sequence and has been reported to be imported into mitochondria[6,7,9]. Although DELE1 has not been structurally characterized experimentally, the amino terminus is predicted to be mostly unstructured, except for a hydrophobic α-helix. The C terminus is predicted to consist of tetratricopeptide repeats (TPRs), comprising 11 α-helices (α1–α11) (Fig. 1a). To gain a better understanding of how DELE1 regulates ISR activity, we initially attempted to express and purify full-length DELE1 and DELE1^{CTD}, the active product of carboxy-terminal cleavage of DELE, using either a bacterial or mammalian expression system, but both systems led to low expression levels and poor solubility. However, expression and solubility of both constructs were improved by fusing a maltose-binding protein (MBP)[10] at the N terminus (Fig. 1a). Recombinant, full-length MBP-DELE1 eluted from a size-exclusion chromatography (SEC) column (Superose 6 Increase 10/300 GL column, see Methods) in a peak volume of ~15 ml, which corresponds to the predicted 96-kDa molecular weight of the monomer (Fig. 1b). However, purified MBP-DELE1^{CTD} eluted in a peak volume of ~11 ml. This corresponds to a molecular weight much larger than that of the 96-kDa monomer, suggesting that this cleaved construct assembles into a higher-order oligomeric species (Fig. 1b). Mass photometry analysis further confirmed that full-length, recombinant MBP-DELE1 is

primarily monomeric (estimated at 92 kDa), whereas the MBP-DELE1^{CTD} sample consisted of species with a higher molecular weight (Extended Data Fig. 1a,b).

We next used single-particle cryo-electron microscopy (cryo-EM) analysis to investigate the oligomeric structure of DELE1^{CTD}. Although negative-stain EM confirmed that the void peak from the SEC column primarily contained cellular debris, the second peak at ~11 ml contained discrete particles that could be further investigated structurally (Fig. 1b). Two-dimensional analysis of the cryo-EM data revealed that MBP-DELE1^{CTD} assembles into an elongated, symmetric oligomer that is ~140 Å in length and ~80 Å in diameter (Extended Data Fig. 2a,b). Fuzzy densities observed at each end of the oligomer likely correspond to the flexible MBP solubilization tags, indicating that MBP-DELE1^{CTD} oligomerizes with the N termini positioned at the periphery of the complex and the C termini directed toward the center (Extended Data Fig. 2b). Three-dimensional analyses confirmed that MBP-DELE1^{CTD} oligomerizes into a mostly hollow cylindrical octamer with D_4 symmetry (Fig. 1c,d and Extended Data Fig. 2b) that exhibits a small degree of inter-subunit, as well as intra-subunit, flexibility. Despite this flexibility, the reconstruction was resolved to a global resolution of ~3.8 Å, which was sufficient to build and refine an atomic model with good confidence (Extended Data Fig. 2b–e and Table 1). The MBP-DELE1^{CTD} octamer assembles as a dimer of two tetramers, in which the N termini from four monomers organize into a crown-like assembly with four-fold symmetry capping each end of the octamer. The TPRs from each monomer extend toward the center to give the oligomer a spring-like appearance. Owing to flexibility of the linker, the MBP moieties were not resolved in the reconstructed density and thus do not impact the organization of the octamer.

Two major interfaces mediate DELE1^{CTD} oligomer formation

The atomic model enabled us to closely examine the specific interactions involved in oligomerization of DELE1^{CTD}. Notably, there are only two sites of inter-protomer interactions involved in oligomerization of active DELE1^{CTD}–one at the N-terminal end (hereafter referred to as interface I), and another near the C terminus of the TPR (hereafter referred to as interface II) (Fig. 2a). The tetrameric crown-like assembly at each end of the complex arises from interactions between the first helices (α1) of four DELE1^{CTD} protomers, where F250 and L251 from one subunit are closely packed with L242 and L239 from the adjacent subunit (Fig. 2b,d and Extended Data Fig. 3b). These hydrophobic interactions, which have an estimated buried surface area of ~518 Å^2, as calculated by the PISA server[11] (Extended Data Fig. 3a), stabilize the four neighboring α1-helices into a weaved, square-shaped arrangement. We posit that the hydrophobic interactions within the α1-helices drives the oligomerization of DELE1 tetramers, and that assembly of the DELE1^{CTD} tetramer positions the C-terminal regions of the TPRs for octamer assembly. Our cryo-EM reconstruction shows that the C-terminal ends of the TPRs engage in an interlocking network of interactions, with a buried surface area of ~504 Å^2 (Extended Data Fig. 3a); these interactions together stabilize the dimer of DELE1^{CTD} tetramers (Fig. 2c). The first of these interactions appears to be a strong hydrogen bond, on the basis of the intensity of the cryo-EM density (Extended Data Fig. 3d) between R403 from the loop preceding the α10-helix and S432 of the α11-helix of the neighboring subunit (Fig. 2e). Next, residues L405 and L409 within the α10-helices from adjacent subunits engage in

symmetrically related hydrophobic interactions facing the lumen of the DELE1^{CTD} cylinder (Fig. 2e and Extended Data Fig. 3e). Last, the F431 residues from the α11-helices of adjacent subunits are positioned for a π-stacking interaction (Fig. 2e and Extended Data Fig. 3c). Together, these interactions form four interlocking, V-shaped assemblies around the equator of the DELE1^{CTD} octamer.

Structure-based alterations disrupt the DELE1 oligomer

Having identified the specific residues involved in stabilization of the DELE1^{CTD} oligomer in our cryo-EM structure, we next sought to probe the biochemical and biophysical relevance of these interactions in DELE1 assembly using mutagenesis. We first aimed to disrupt the interactions at interface II, which are involved in dimerization of DELE1^{CTD} tetramers according to our cryo-EM structure. This was achieved by introducing two substitutions: p.R403A, which we anticipated would disrupt the inter-subunit hydrogen bonding suggested by our atomic model, and p.F431S, which would abolish the inter-subunit π-stacking interactions. These alterations were cloned into the same MBP-DELE1^{CTD} fusion vector that was used for the wild-type (WT) DELE1^{CTD}. The SEC chromatogram of this double mutant confirmed our hypothesis that disrupting the interactions at interface II would compromise octamer assembly, as we observed formation of an oligomeric species that was smaller than that observed for WT DELE1^{CTD} (Fig. 3a). Sodium dodecyl sulfate–polyacrylamide gel electrophoresis (SDS–PAGE) of the SEC peak fractions confirmed the presence of DELE1^{CTD}-R403A F431S (Fig. 3h). We also used negative-stain EM to confirm that DELE1^{CTD}-R403A F431S prevents assembly of the octameric species, instead forming smaller oligomers that are consistent with DELE1^{CTD} tetramers (Extended Data Fig. 4c,d).

We next mutated the four residues within the α1-helix that we identified as important for assembly of the tetrameric N-terminal crowns of the DELE1^{CTD} octamer. We also removed a portion of the α1-helix by truncating the N terminus to V244 (Δ244), which will completely disrupt the hydrophobic core at interface I. As shown in Figure 3b–g, individual or combined substitutions at the N terminus, as well as the Δ244 truncation, disrupted DELE1^{CTD} oligomerization in vitro, as demonstrated by SEC chromatograms of the mutant proteins corresponding to monomeric or dimeric species (Fig. 3b–g and Extended Data Fig. 1c). The presence of the mutants was validated by SDS–PAGE of the respective SEC peak fractions (Fig. 3h), and mass photometry of the Δ244 mutant confirmed that the species in the sample was homogeneously monomeric (Extended Data Fig. 1c). We further confirmed the abolishment of higher-order oligomerization by visualizing the mutant proteins with negative-stain EM (Extended Data Fig. 4e). Together, these data support an assembly model wherein hydrophobic interactions at interface I promote formation of the DELE1^{CTD} tetramers, and these tetramers dimerize via interactions at interface II. Notably, none of these substitutions are predicted by AlphaFold2 to affect the overall fold of the DELE1^{CTD} monomer (Extended Data Fig. 4a,b), indicating that although these alterations impact DELE1^{CTD} oligomerization, the disruptions are likely not due to perturbed folding or stability of the protein.

Having demonstrated the role of the indicated residues at interfaces I and II in oligomerization in vitro using recombinantly purified MBP-tagged proteins, we next

examined the impact of substitutions on DELE1^{CTD} oligomerization in mammalian cells. To accomplish this, we overexpressed WT DELE1^{CTD} and DELE1^{CTD} mutants in HEK293T cells and used sucrose gradient sedimentation to assess their oligomerization state in cell lysates. Given the lack of effective, commercially available antibodies that can be used to detect the DELE1 protein by immunoblotting[6], we introduced a green fluorescent protein (GFP) tag at the C terminus of DELE1^{CTD} and used an anti-GFP antibody to detect the DELE-GFP fusion protein. Although WT DELE1^{CTD} was detected across a wide range of the gradient fractions, the majority of the protein migrated to the high-molecular-weight fractions (Fig. 3i), confirming formation of DELE1^{CTD} oligomers in cells. The presence of smaller oligomeric species or monomers was expected, as we observed similar oligomeric heterogeneity for WT DELE1^{CTD} in our EM images (Extended Data Fig. 2a). The interface II mutant (DELE1^{CTD}-R403A F431S) retained some oligomeric species, as expected on the basis of the tetramerization of this mutant in vitro (Fig. 3a,i), but the substitutions in interface I resulted in a notable shift of the proteins to lighter fractions of the gradient relative to the WT protein (Fig. 3i), consistent with our in vitro data (Fig. 3a–h and Extended Data Fig. 4c,d). We further confirmed the oligomerization of DELE1^{CTD} in HEK293T cells using a GFP-tagged construct by fluorescence-detection SEC (FSEC). As expected, a large percentage of the WT DELE^{CTD}-GFP eluted in high-molecular-weight fractions, whereas the oligomerization-deficient Δ244 mutant eluted in small-molecular-weight fractions (Extended Data Fig. 4f). Taken together, these results indicate that the cleaved form of DELE1 oligomerizes in mammalian cells and that this oligomerization is mediated by localized interactions at two sites within the protein.

Assembly-deficient DELE1^{CTD} show impaired activation of the ISR signaling

We next sought to define the specific importance of DELE1^{CTD} oligomerization for ISR activation. Overexpressing DELE1^{CTD}-mClover induces HRI-dependent increases in the ISR-regulated protein ATF4 (ref. 6), and we hypothesized that overexpressing oligomerization-deficient DELE1^{CTD}-mClover interface I and interface II mutants would abolish this ATF4 upregulation. To confirm similar levels of DELE1^{CTD} expression, we monitored protein levels by immunoblotting (Fig. 4a and Extended Data Fig. 5a). We found that interface I triple and quadruple mutants, as well as the interface I Δ244 mutant, demonstrated higher basal levels of DELE1^{CTD} than did wild-type protein. By contrast, the interface II double mutant and the interface I double mutant showed lower levels of expression, likely reflecting reduced stability. In accordance with previous results, we observed increased ATF4 in HEK293T cells overexpressing DELE1^{CTD}-mClover (Fig. 4a,b). Despite lower levels of expression (Fig. 4a), overexpression of DELE1^{CTD}-mClover-R403A F431S, which harbors the substitutions that lead to DELE1 tetramer formation (Fig. 3a,i and Extended Data Fig. 4d), increases ATF4 expression in HEK293T cells to levels similar to those observed for the wild-type protein (red in Fig. 4a,b). By contrast, overexpression of DELE1^{CTD} interface I mutants that fully disrupt DELE1 oligomerization in vitro and in cells (Fig. 3b–g,i and Extended Data Fig. 4e) do not increase ATF4 protein levels (purple in Fig. 4a,b). Analogous results were observed in HEK293T cells stably expressing an ATF4-FLuc ISR translational reporter (Extended Data Fig. 5b) transfected with DELE1^{CTD}-GFP constructs containing interface I and II substitutions (Fig. 4c). The

HRI activator BtdCPU[12] is shown as a control. Together, our results suggest that disruption of DELE1^{CTD} oligomerization prevents DELE1^{CTD}-dependent ISR activation.

Recent results have shown that full-length DELE1 can accumulate in the cytosol and activate HRI-dependent ISR signaling in response to specific types of stress[9,13]. This suggests that full-length DELE1 should similarly assemble into oligomers to promote ISR activation. Although recombinant full-length DELE1 did not oligomerize in vitro (Fig. 1b and Extended Data Fig. 1a), both full-length and C-terminally-truncated DELE1-mClover migrated as oligomers in sucrose gradients of lysates prepared from HEK293T cells transiently transfected with full-length DELE1 (Extended Data Fig. 5d). This indicates that full-length, mature DELE1 can integrate into oligomers. Further, we found that overexpression of full-length DELE1 robustly activated the ATF4-FLuc ISR reporter in HEK293T cells (Fig. 4d). Similar activity was observed for full-length DELE1 harboring the interface II substitutions p.R403A and p.F431S. However, interface I mutants prevented the ATF4-FLuc activation afforded by DELE1 overexpression. Collectively, these results indicate that both full-length DELE1 and DELE1^{CTD} can integrate into oligomers to initiate ISR signaling, and their ability to induce ISR is compromised by oligomerization-deficient mutants.

Interface I mutants disrupt HRI activity

Previous results have shown that DELE1^{CTD} binds to HRI to induce its activation[6,7]. Thus, we next sought to define whether HRI interaction with DELE1^{CTD} is dependent on oligomerization. We co-overexpressed FLAG-HRI and DELE1^{CTD}-GFP mutants in HEK293T cells and monitored the recovery of DELE1^{CTD} in FLAG immunoprecipitations (IPs). Surprisingly, all DELE1^{CTD} mutants efficiently co-immunoprecipitated with FLAG-HRI (Extended Data Fig. 6a). This result suggests that DELE1^{CTD} mutants are properly folded and that DELE1 binding to HRI does not require DELE1 oligomerization.

We next sought to further define the interaction between DELE1 and HRI. The kinase domains of the four kinases involved in ISR activation (HRI, PERK, PKR, and GNC) are homologous, but each contains a unique N-terminal domain (Extended Data Fig. 6b,c). We generated FLAG-tagged constructs of the full-length HRI, the unique HRI N-terminal domain (HRI^{NTD}, residues 1–160), and the homologous C-terminal kinase domain (HRI^{CTD}, residues 161–630) (Extended Data Fig. 6b,d). We then co-expressed these constructs with DELE1^{CTD}-GFP in HEK293T cells and monitored interactions between these proteins by IP and immunoblotting. We found that both full-length HRI and the HRI^{NTD}, but not the HRI^{CTD}, efficiently co-immunoprecipitated with DELE1^{CTD}-GFP (Extended Data Fig. 6d,e). This suggests that DELE1^{CTD} interacts with HRI through its unique N-terminal domain and not the highly conserved kinase domain (Extended Data Fig. 6c). This finding is consistent with a mechanism by which HRI can be distinctly recognized by DELE1, while retaining the ability to activate a common substrate, eIF2α, through a conserved kinase domain.

To further probe the involvement of DELE1 in promoting HRI activity, we co-expressed FLAG-tagged HRI and DELE1^{CTD}-mClover in HEK293T cells. We then monitored active, phosphorylated HRI and phosphorylation of the HRI substrate eIF2α by immunoblotting. We confirmed that lysates prepared from cells co-expressing wild-type HRI and wild-type

DELE1^{CTD}-mClover showed both phosphorylated HRI and eIF2α (Fig. 4e,f and Extended Data Fig. 5c). Importantly, phosphorylated HRI and eIF2α were not observed in cells co-expressing a kinase-dead (p.H440N) HRI and wild-type DELE1^{CTD}-mClover. Similarly, treatment of lysates prepared from HEK293T cells co-expressing wild-type HRI and wild-type DELE1^{CTD}-mClover with lambda phosphatase ablated phosphorylation of HRI and eIF2α (Fig. 4e,f). Together, these results confirm that the observed bands reflect phosphorylation induced by HRI kinase activity. Co-overexpression of wild-type HRI with the the tetrameric interface II double mutant DELE1^{CTD}-R403S F431S resulted in levels of HRI and eIF2α phosphorylation similar to those observed for wild-type DELE1^{CTD} (Fig. 4e,f and Extended Data Fig. 5c). This is consistent with the efficient activation of ATF4 signaling observed with this mutant (Fig. 4a–c) and indicates that DELE1^{CTD} tetramerization is sufficient to induce HRI activation and subsequent eIF2α phosphorylation. Intriguingly, while only some of the interface I mutants that impair DELE1 oligomerization and ISR activation show diminished HRI autophosphorylation (Fig. 4e and Extended Data Fig. 5c), all of these mutants notably decrease eIF2α phosphorylation (Fig. 4e,f). This suggests that DELE1 oligomerization disrupts HRI enzymatic activity, potentially by serving as a platform to promote DELE1–HRI–eIF2α interactions or by directly influencing the activity of this kinase.

Discussion

DELE1 has previously been identified to function as a messenger protein relaying mitochondrial stress to the ISR, enabling a robust and precise cellular response to various mitochondrial perturbations. Our studies suggest that cytosolic DELE1 assembles as an oligomer that is required to initiate downstream ISR signaling. Given the bioenergetic demands of mitochondria and their dynamic relationship to cellular function, DELE1-dependent ISR activation must be tightly controlled to prevent activation under resting conditions but also allow rapid triggering to counter insults associated with physiopathological stresses[2,14–17]. Our findings reveal a molecular mechanism that enables the precise regulation of DELE1-mediated stress signaling under diverse cellular conditions wherein DELE1 oligomerization serves as a molecular signal to activate the ISR.

The importance of DELE1 oligomerization suggests new potential mechanisms that could distinctly regulate ISR signaling through this pathway in response to diverse types of pathological insults. Post-translational DELE1 modification or altered interaction with cytosolic factors that influence DELE1 oligomer stability could directly promote or suppress ISR activity. Further, although full-length DELE1 and DELE1^{CTD} both incorporate into oligomers, differences in the stability or regulation of these distinct oligomer populations could enable adjustments in the extent and duration of DELE1-mediated ISR signaling in response to the mitochondrial insults. Consistent with this, we show that full-length MBP-DELE1 does not readily assemble into oligomers in vitro (Fig. 1b), suggesting that this protein may be less effective than DELE1^{CTD} at oligomerization. Regardless, overexpression of full-length DELE1 in cells leads to DELE1 oligomerization and ISR activation; however, this increase in ISR signaling induced by full-length DELE1 is diminished by DELE1 oligomerization mutants. This further indicates that oligomerization of DELE1—whether full-length, cleaved, or a mixture of the two—is required for activation

of the ISR upon mitochondrial stress. Although the potential to regulate DELE1-dependent ISR signaling through post-translational regulation of DELE1 oligomerization remains to be further explored, our study suggests that modulation of ISR signaling through DELE1 oligomerization enables tuning of the DELE1-mediated response to varying levels and types of cellular stress. We used a cell-based overexpression system to examine the role of DELE1 oligomerization owing to a lack of effective commercial antibodies that can detect endogenous DELE1, but these findings establish a strong foundation for future investigation into the role of DELE1 oligomerization in physiological conditions.

Earlier studies have shown that cleaved DELE1 directly binds HRI to become activated, but the specific impact of DELE1 binding on HRI activity was previously poorly understood. Here we show that WT and oligomerization-deficient DELE1 mutants all have the capacity to bind HRI, but oligomerization-deficient mutants diminish HRI-mediated phosphorylation of eIF2α and subsequent ISR activation. This suggests that DELE1 functions as a template for HRI activity. Other ISR-associated kinases, such as PKR, undergo ligand-induced dimerization for *trans*-autophosphorylation and enzymatic activation[18,19]. It is plausible that HRI may use a similar activation mechanism, whereby DELE1^{CTD} oligomerization produces a signaling platform that is a scaffold for HRI activity. Further structural investigation into the details of the DELE1–HRI interaction and how these interactions mediate HRI kinase activity will establish a more complete mechanistic understanding of the molecular signaling linking mitochondrial stress to the ISR. Recent studies have identified that PKR clustering through phase separation is another novel regulatory mechanism for fine-tuning downstream ISR activation[20]. It remains to be seen whether a similar mechanism is shared by the DELE1–HRI–eIF2α axis upon mitochondrial stress.

Rapid and efficient transduction of mitochondrial stress to activate the ISR is an essential component of cellular homeostasis maintenance, and dysregulation of this pathway has been observed in a wide range of human diseases[14–16,21]. It has proven particularly challenging to target mitochondrial function in the context of pathological conditions owing to the double-membrane barrier of the organelle and its dynamic morphology. DELE1 functions as a bridging effector of mitochondrial stress with access to the cytosol, positioning it as an attractive target for therapeutic purposes. Our description of the DELE1^{CTD} oligomer and its relevance to the ISR pathway provides a potentially serendipitous avenue to target DELE1 activity specifically and to subsequently tune adaptive ISR signaling for therapeutic intervention to counter human mitochondrial pathologies without impacting the cellular capacity to respond to other stresses, such as endoplasmic reticulum stress or viral infections.

Methods

Reagents, plasmids and cell lines

BtdCPU compounds were purchased from Fisher Scientific. The DELE1 cDNA was from GenScript. The anti-eGFP monoclonal antibody (F56–6A1.2.3) was purchased from Abcam. The anti-ATF4 monoclonal antibody was purchased from Cell Signaling (D4B8). The anti-GAPDH monoclonal antibody (sc-47724) was from Santa Cruz Biotechnology. The mouse anti-FLAG antibody (F1804) was purchased from Sigma-Aldrich. The rabbit

anti-FLAG antibody (no. 14793) was purchased from Cell Signaling. The anti-eIF2α antibody (AHO0802) was purchased from Thermo Fisher Scientific. The anti-phospho-eIF2α antibody (no. 3398) was purchased from Cell Signaling. The anti-β-tubulin antibody (10094-1-AP) was purchased from Proteintech. The secondary antibodies against mouse and rabbit IgG were purchased from LI-COR Biosciences, and all antibodies were diluted according to the manufacturer's instructions. The sequences of primers used for cloning are reported in Supplementary Table 1. The Gibson assembly method (NEB E2611) was used for all cloning experiments. The Q5 site-directed mutagenesis kit from New England Biolabs was used to generate the DELE1 mutants. The full-length DELE1 (M1-G515), DELE1^{CTD} (K225-G515), and mutants for recombinant protein expression were cloned into a modified pET22b bacterial expression vector, which was shared by T. S. Xiao (Case Western Reserve University, Cleveland). The vector contains a non-cleavage MBP tag at the N terminus and 6×-His tag at the C terminus. For mammalian expression, DELE1 constructs were cloned into a modified pcDNA3.1 vector, which contains a GFP tag at the C terminus. A six-residue Gly-Ser linker was engineered between DELE1 and the GFP tag. The HEK293T cell line was from American Type Culture Collection CRL-3216. The ATF4-luciferase translational reporter cell line (ATF4-FLuc) was generated through the adaption of the previously published ATF4-mAPPLE reporter cell line[6]. In brief, we replaced the mApple with firefly luciferase and stably transfected this reporter into HEK293T cells. Next, we selected a clonal cell line that showed robust activation of ATF4-Fluc upon treatment with various ISR activators, including oligomycin A (OA) and thapsigargin (Tg), demonstrating that the reporter cells can accurately report on ISR activation induced by multiple stressors.

Protein expression and purification

The full-length DELE1, DELE1^{CTD}, and mutants were all expressed and purified using a similar methodology. *Escherichia coli* strain BL21 (DE3) Codon Plus RIPL (Agilent Technologies) was used for recombinant DELE1 protein expression. The transformed BL21 RIPL cells were grown at 37 °C until the OD reached ~0.8, and protein expression was induced with 1 mM IPTG at 16 °C overnight. Cells were collected by centrifugation at 5,000*g* for 30 min at 4 °C. The cell pellets of the DELE1^{CTD} and mutants were resuspended and lysed using sonication in a lysis buffer containing 25 mM Tris-HCl (pH 8.0), 500 mM NaCl, 10% glycerol, and 100 μM PMSF and were lysed using sonication. The lysate was cleared by ultracentrifugation at 30,000*g* for 30 min at 4 °C, followed by Ni-NTA affinity binding. The column was washed with lysis buffer supplemented with 25 mM imidazole (10 column volumes) and 50 mM imidazole (5 column volumes), respectively. Right after washing, the protein was eluted with elution buffer containing 25 mM Tris-HCl (pH 8.0), 500 mM NaCl, 10% glycerol, and 300 mM imidazole. Full-length DELE1 was mostly insoluble when prepared using the purification protocol used for DELE1^{CTD}, but solubility was rescued by including 1% *n*-dodecyl-ß-D-maltoside (DDM) detergent in the buffer. The cells were resuspended and sonicated in the same lysis buffer as DELE1^{CTD}, and then solubilized and extracted from membranes by adding 1% DDM detergent while stirring at 4 °C for 1 h. The lysate containing solubilized DELE1 was clarified by ultracentrifugation at 45,000*g* for 1 h at 4 °C, followed by Ni-NTA affinity binding. The column was washed with lysis buffer supplemented with 0.1% DDM and 25 mM imidazole (10 column volumes), and

eluted with lysis buffer supplemented with 0.1% DDM and 300 mM imidazole. All proteins were further purified through SEC using a Superose 6 increase column. The SEC buffer for WT DELE1^{CTD} and the mutants contained 25 mM Tris-HCl (pH 8.0), 150 mM NaCl, 5% glycerol, and 5 mM DTT. The SEC buffer for full-length DELE1 is the above buffer supplemented with 0.1% DDM. Peak fractions containing the target proteins were pooled, concentrated, aliquoted, and flash-frozen in liquid nitrogen for storage at −80 °C.

Sample preparation for electron microscopy

For negative-stain electron microscopy, 4 μl of DELE1 samples at 0.1 mg ml^{-1} were applied onto carbon coated 400 mesh Cu-Rh maxtaform grids (Electron Microscopy Sciences), which were plasma cleaned for 15 s using the Pelco glow discharge cleaning system (Ted Pella) with atmospheric gasses at 15 mA. The samples were stained using 2% (wt/vol) uranyl formate solution, then blotted and dried. For cryo-EM, 4 μl of WT DELE1^{CTD} sample at 3 mg ml^{-1} was applied onto 300 mesh R1.2/1.3 UltraAuFoil holey gold grids (Quantifoil) that were plasma cleaned for 15 s using Pelco glow discharge cleaning system (Ted Pella) with atmospheric gasses at 15 mA. The grids were immediately vitrified by plunge-freezing using a Thermo Fisher Vitrobot Mark IV at 4 °C, 5 s, 100% humidity, and a blot force of 0 using Whatman grade 1 blotting paper.

Cryo-EM data collection and processing

Single-particle cryo-EM data were collected on a Thermo Fisher Talos Arctica transmission electron microscope operating at 200 keV using parallel illumination conditions[23,24]. Micrographs were acquired using a Gatan K2 Summit direct electron detector, with a total electron exposure of 50 e^{-} Å^{-2} as a 49-frame dose-fractionated movie during a 9,800-ms exposure time. The Leginon data collection software[25] was used to collect a total of 13,164 micrographs during multiple sessions at 36,000 nominal magnification (1.15 Å pixel^{-1}) with a nominal defocus ranging from −0.7 μm to −1.2 μm. Stage movement was used to target the center of either 4 or 16 1.2-μm holes for focusing, and image shift was used to acquire high magnification images. The Appion image processing wrapper[26] was used to run MotionCor2 for real-time micrograph frame alignment and dose-weighting during data collection[27]. All subsequent image processing was performed in cryoSPARC[28]. The contrast transfer function (CTF) of each image was estimated using CTFFind4 and Patch CTF estimation (multi) within cryoSPARC using default parameters. Blob picking on a small portion of the CTF estimated images (~200 images) using a particle diameter of 150 Å to 250 Å was used for initial particle picking. The picked particle coordinates were extracted at 1.15 Å pixel^{-1} from the motion-corrected and dose-weighted micrographs using a box size of 256 pixels, followed by two-dimensional (2D) classification into 50 classes using default parameters. Representative views of 2D classes from the initial processing were used as templates for template-based particle picking in cryoSPARC, which resulted in ~1.06 million particle selections. After inspecting the picked particles, 660,425 picked particle coordinates with an NCC score above 0.180 and local power between 85 and 166 were extracted at 1.15 Å pixel^{-1} from the motion-corrected and dose-weighted micrographs using a box size of 256 pixels. The extracted particles were 2D classified into 100 classes using default cryoSPARC parameters, and the 92,455 particles contributing to the 2D classes displaying high-resolution secondary structural features were selected for further

processing. A reference-free three-dimensional (3D) ab initio model was generated using default parameters and used for non-uniform refinement with C_1 symmetry. The resulting reconstruction, which was resolved to 5.4 Å resolution according to the Fourier Shell Correlation (FSC) at a cutoff of 0.143, exhibited secondary structural features that were consistent with a D_4 symmetry. Another round of non-uniform refinement was performed using the same ab initio model, but D_4 symmetry was imposed. Heterogeneous refinement with D_4 symmetry was then used to classify the particles into three classes, and the 67,067 particles contributing to the two classes containing higher resolution features were combined and then subjected to a final round of non-uniform refinement with D_4 symmetry. This final refinement produced the final reconstruction at a reported global resolution of 3.8 Å at an FSC cutoff of 0.143. CTF refinement in cryoSPARC did not improve the resolution of the reconstruction. Directional FSCs were estimated by the 3DFSC server[29] (Extended Data Fig. 1).

Atomic model building and refinement

The AlphaFold2 model of DELE1 (Extended Data Fig. 3a) was initially docked into the reconstructed density map using UCSF Chimera. Real-space structural refinement and manual model building were performed with Phenix[30] and Coot[31], respectively. Phenix real-space refinement included global minimization, rigid body, local grid search, atomic displacement parameters, and morphing for the first cycle. It was run for 100 iterations and five macro cycles, with a target bonds root mean square deviation (r.m.s.d.) of 0.01 and a target angles r.m.s.d. of 1.0. The refinement settings also included secondary structure and Ramachandran restraints. Figures were prepared using UCSF Chimera[28] and UCSF ChimeraX[32,33]. Data collection, refinement, and validation statistics are summarized in Table 1.

Sucrose gradient sedimentation

HEK293T cells at approximately 50% confluency on a 10-cm dish were transfected with 5 μg of DELE1 plasmid using the calcium phosphate method, and the proteins were expressed for 24 h post-transfection. The cells were pelleted at 600*g* for 5 min at 4 °C and washed twice with 10 ml of PBS buffer. The final cell pellet was resuspended in 250 μl of lysis buffer (10 mM Tris/HCl pH 7.5, 150 mM NaCl, 0.5 mM EDTA, 0.5% (vol/vol) NP-40, 5% (vol/vol) glycerol, Roche complete protease inhibitors) and incubated on ice for 25 min. The lysate was then clarified by centrifugation at 21,000*g* for 10 min at 4 °C and added on top of a 4-ml continuous 10–30% (wt/wt) sucrose gradient in TBS (25 mM Tris-HCl/150 mM NaCl, pH 7.2). This was followed by centrifugation in a SW60Ti rotor at 33,000 r.p.m. (146,334*g*) for 18 h at 4 °C. The gradient was manually fractionated from the top into 0.2-ml fractions. The presence of DELE1 proteins in sucrose fractions was assessed by immunoblotting using an anti-GFP antibody.

Luciferase assay

ATF4-Fluc cells were transfected with 5 μg of each DNA using calcium phosphate. The medium was replaced with fresh medium the morning after transfection. Sixteen hours post-transfection, cells were seeded at 15,000 cells per well into both white and clear 96-well plates for luciferase and viability assays. Forty hours post-transfection, mock-transfected

cells were treated with DMSO or 10 μM BtdCPIU for 8 h. Following drug treatment, Bright-Glo reagent was added to each well at a 1:1 ratio with respect to the medium volume. Cells were lysed for 10 min at room temperature, and the luminescence signal was read on a Tecan machine with an integration time of 1,000 ms.

DELE1 rescue experiments in DELE1 knockdown cells

Different DELE1 variants fused with GFP were transfected using Mirus TransIT-LT1 Transfection Reagent (MIR2304) into ATF4 reporter cells with about 50% of cell population having knockdown (KD) of DELE1 by CRISPRi. The DELE1 KD cells were generated by expressing a *DELE1* single guide RNA and a blue fluorescent protein (BFP) marker[6]. Twenty-four hours post-transfection, cells were seeded in a 96-well plate at about 25% confluency. The following day, oligomycin at a final concentration of 1.25 ng ml^{-1} was added for 16 h. After treatment, the cells were sorted into four populations, including $BFP^{+}GFP^{+}$ DELE KD, $BFP^{+}GFP^{-}$ DELE KD, DELE1 KD $BFP^{-}GFP^{+}$, and $BFP^{-}GFP^{-}$ DELE1 KD. The ATF4 reporter level for each population of cells was measured using flow cytometry.

Co-immunoprecipitation

To analyze the interaction between HRI and DELE1 mutants. HEK293T cells were transiently transfected with 5 μg of FLAG-tagged full-length HRI construct and 5 μg of GFP-tagged DELE1 constructs ($DELE1^{CTD}$ or mutants) using lipofectamine 3000 transfection reagent (L3000008, Thermo Fisher Scientific). GFP empty vector was used as a negative control. To study the interaction between DELE1 and HRI NTD (residues 1–160) and DELE and HRI CTD (residues 161–630), HEK293T cells were transiently transfected with 5 μg of mClover-tagged $DELE1^{CTD}$ and 5 μg of FLAG-tagged full-length HRI, FLAG-tagged HRI NTD, and FLAG-tagged HRI CTD constructs. Cells were collected 24 h after transfection and lysed using a lysis buffer (25 mM Tris/Cl pH 7.5, 150 mM NaCl, 0.5 M EDTA, 0.5% NP-40, 2.5% glycerol, and Roche cOmplete Protease Inhibitors). The lysates were then incubated with 15 μl anti-FLAG M2 magnetic beads (M8823, Sigma-Aldrich) for 3 h at 4 °C. Samples were washed three times with wash buffer (25 mM Tris-HCl, 150 mM NaCl, 0.1% NP-40). Proteins captured on the magnetic beads were eluted with 2× SDS loading dye for 5 min and analyzed by western blotting using rabbit anti-FLAG (14793S; Cell Signaling Technology) and anti-GFP (A-6455, Thermo Fisher Scientific) to detect HRI-FLAG and DELE1-GFP, respectively.

Western blotting

For the ATF4 immunoblotting assay, HEK293T cells were transiently transfected with 5 μg of our DELE1 constructs ($DELE1^{CTD}$ or mutants) using calcium phosphate. Cells were lysed 24 h post-transfection using the RIPA lysis buffer (89900, Thermo Fisher Scientific) supplemented with Roche protease inhibitors. The total protein concentrations were measured by Bradford protein assay (Bio-Rad). Protein samples were separated by sodium dodecyl sulfate–polyacrylamide gels and transferred onto nitrocellulose membranes. An anti-ATF4 antibody (D4B8, Cell Signaling Technology) was used to detect the ATF4 levels in each sample. For the HRI and eIF2α phosphorylation assay, 5 μg of FLAG-tagged full-length HRI constructs (WT or H440N mutant) and 5 μg of mClover-tagged DELE1

constructs (DELE1^{CTD} or mutants) were co-transfected into HEK293T cells using the Lipofectamine 3000 transfection reagent (L3000008, Thermo Fisher Scientific). Cells were lysed 8 h post-transfection using the Pierce IP lysis buffer (87788, Thermo Fisher Scientific) supplemented by Roche complete protease inhibitors. The negative control lysis was treated with lambda phosphatase for 30 min at 30 °C. The protein concentrations were measured by Bradford protein assay (Bio-Rad). Protein samples were separated by sodium dodecyl sulfate–polyacrylamide gels and transferred onto nitrocellulose membranes. The proteins were detected by an anti-FLAG antibody (14739, Cell Signaling Technology), anti-p-eIF2α antibody (3398, Cell Signaling Technology), anti-eIF2α antibody (AHO0802, Invitrogen), antimClover antibody (NB600–308, Novus Biologicals), or anti-GAPDH antibody. Digital images were acquired using the LI-COR Image Studio Software.

Mass photometry

Mass photometry experiments were carried out on a Refeyn's second-generation mass photometer instrument. Microscope cover glasses (no. 1.5H, 24 × 50 mm^2) were cleaned with milli-Q H_2O, isopropanol, and milli-Q H_2O again, then dried with clean nitrogen gas. The sample wells were assembled by applying double-sided sticky gasket strips on the cleaned glasses. For each acquisition, 20 μl of sample (15 μl buffer + 5 μl protein) was applied into a fresh well, and movies of 60 s duration were recorded. Autofocus stabilization was done right before each acquisition using 15 μl buffer. The final concentrations for proteins sample were in a range of 5–200 nM. The DiscoverMP (Refeyn) software was used for image analysis and data processing. BSA and thyroglobulin were used as MW standards. The mass photometry experiments were done in triplicate.

Fluorescence-detection size-exclusion chromatography

GFP-tagged DELE1 constructs were expressed in HEK293T cells for 24 h post-transfection. Cells were lysed using a lysis buffer containing 25 mM Tris/Cl pH 7.5, 150 mM NaCl, 0.5 M EDTA, 0.5% NP-40, 2.5% glycerol, and Roche cOmplete Protease Inhibitors. The lysates were cleaned by centrifugation at 40,000*g* for 30 min at 4 °C, which were further filtered before loading to the FSEC system (Agilent Technologies). Then 100 μl of each lysate was applied to a Superose 6 Increase 10/300 GL column (GE Healthcare) equilibrated with buffer containing contained 25 mM Tris-HCl (pH 8.0), 150 mM NaCl, 5% glycerol, and 5 mM DTT. GFP signals were detected in a fluorescence detector using 488 nm for excitation and 510 nm for emission.

Reporting summary

Further information on research design is available in the Nature Portfolio Reporting Summary linked to this article.

Extended Data

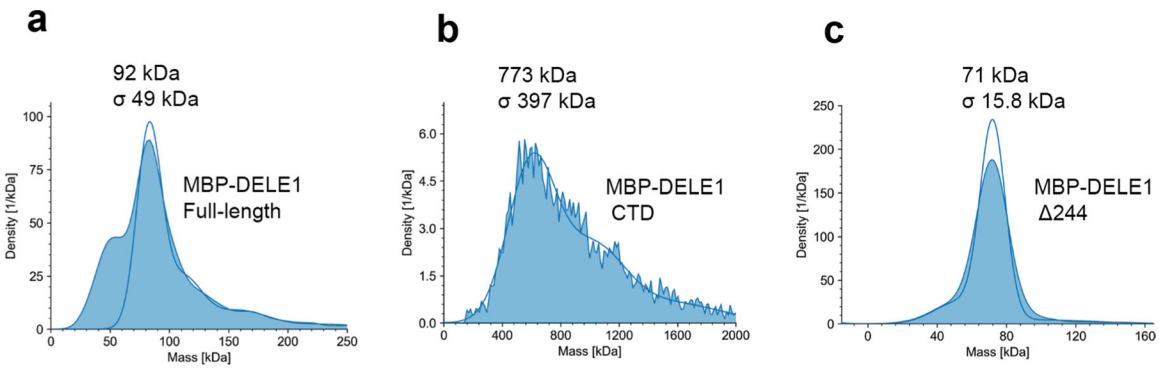

Extended Data Fig. 1 |. Mass photometry of recombinant MBP-DELE1 proteins.

Mass distribution histograms obtained using mass photometry for (**a**) full-length MBP-DELE1, (**b**) MBP-DELE1 CTD, and (**c**) MBP-DELE1 Δ244 truncation. The calculated molecular weight (MW) at the peak for each histogram is shown. BSA and thyroglobulin were used as MW standards for calibrations. Data shown are representative of experiments that were performed in triplicate or more.

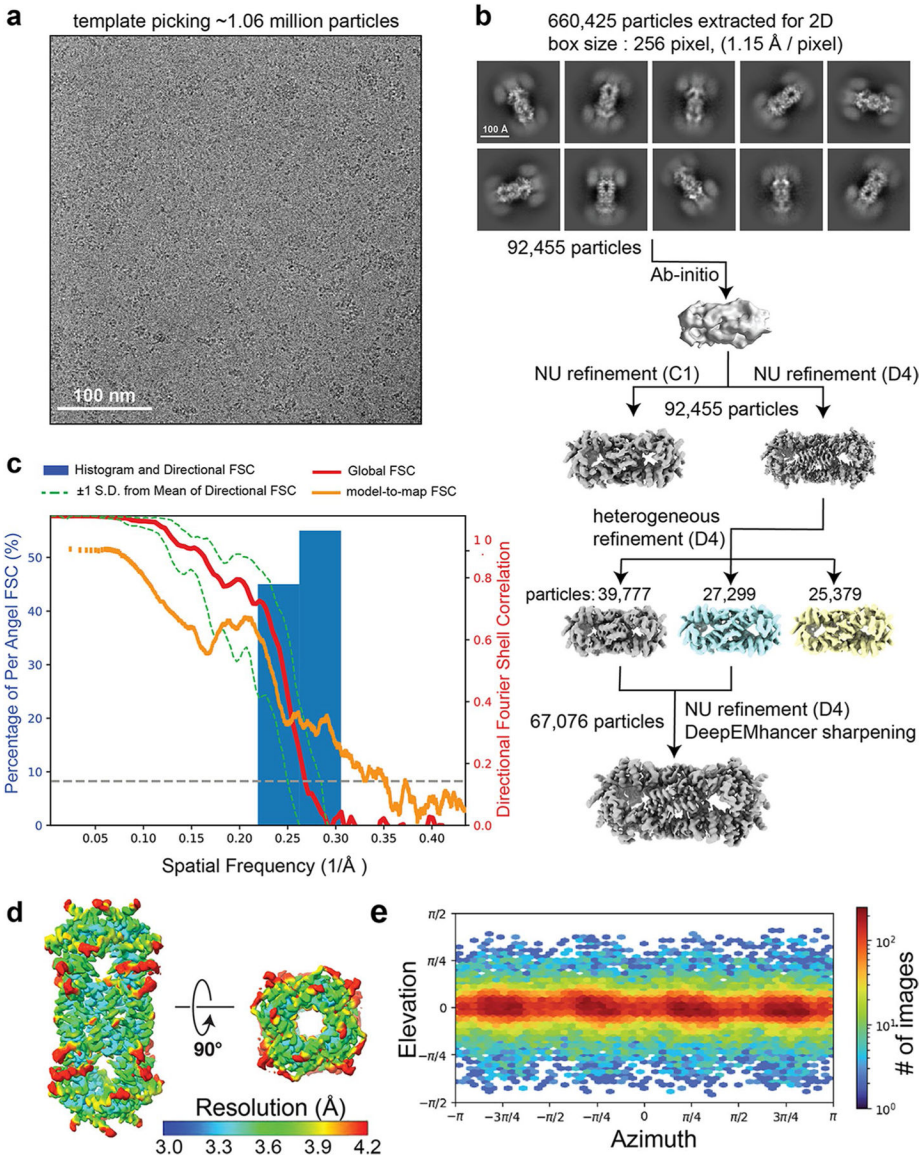

Extended Data Fig. 2 |. Cryo-EM structure determination of DELE1.

a, Representative micrograph of cryo-EM data collection. A total of 13,164 micrographs were collected. The high background on the micrograph appears to be the monomeric or small oligomeric species of DELE1^{CTD}, possibly caused by denaturing due to interaction with the air-water interface during cryofreezing[34,35], although there may be oligomeric heterogeneity within the sample prior to freezing. **b**, Cryo-EM data processing workflow using CryoSPARC software. The final 3D reconstruction map was used for model building and refinement. **c**, 3D Fourier Shell Correlation (3DFSC)[29] of the final reconstruction reporting a global resolution at ~3.8 Å and high level of resolution isotropy, with the FSC at 0.143 denoted. The model-to-map FSC plot from Phenix real space refinement is overlaid. **d**, Final reconstruction filtered and colored by local resolution, as estimated in CryoSPARC. **e**, Euler angle distribution plot of the particles used in the final 3D reconstruction showing complete tomographic coverage of projections.

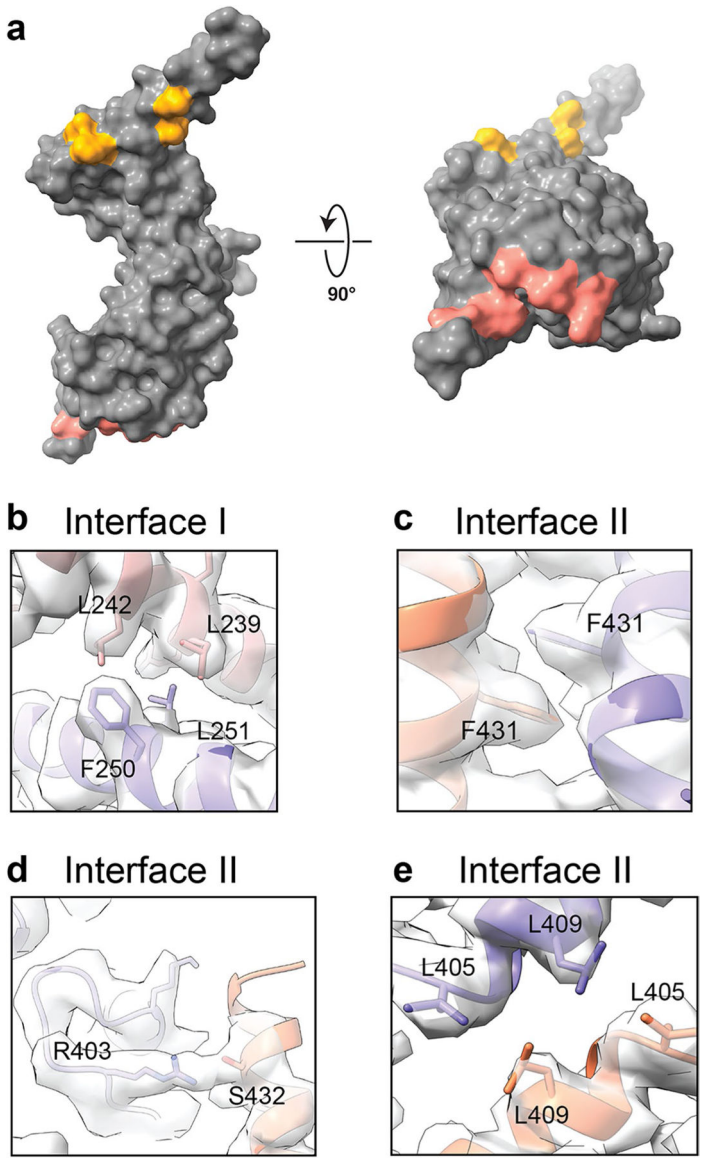

Extended Data Fig. 3 |. Inter-subunit interactions among the DELE1 oligomer.

a, A surface representation of the DELE1^{CTD} monomer is shown in two orthogonal views, colored gray. The buried surface areas associated with oligomerization Interfaces I and II are colored orange and salmon, respectively. **b-e**, Detailed views of the Interface I and II interactions demonstrating the quality of the cryo-EM density, which is shown as transparent surface. The interacting residues are shown as sticks, and the coloring is consistent with that of Fig. 2.

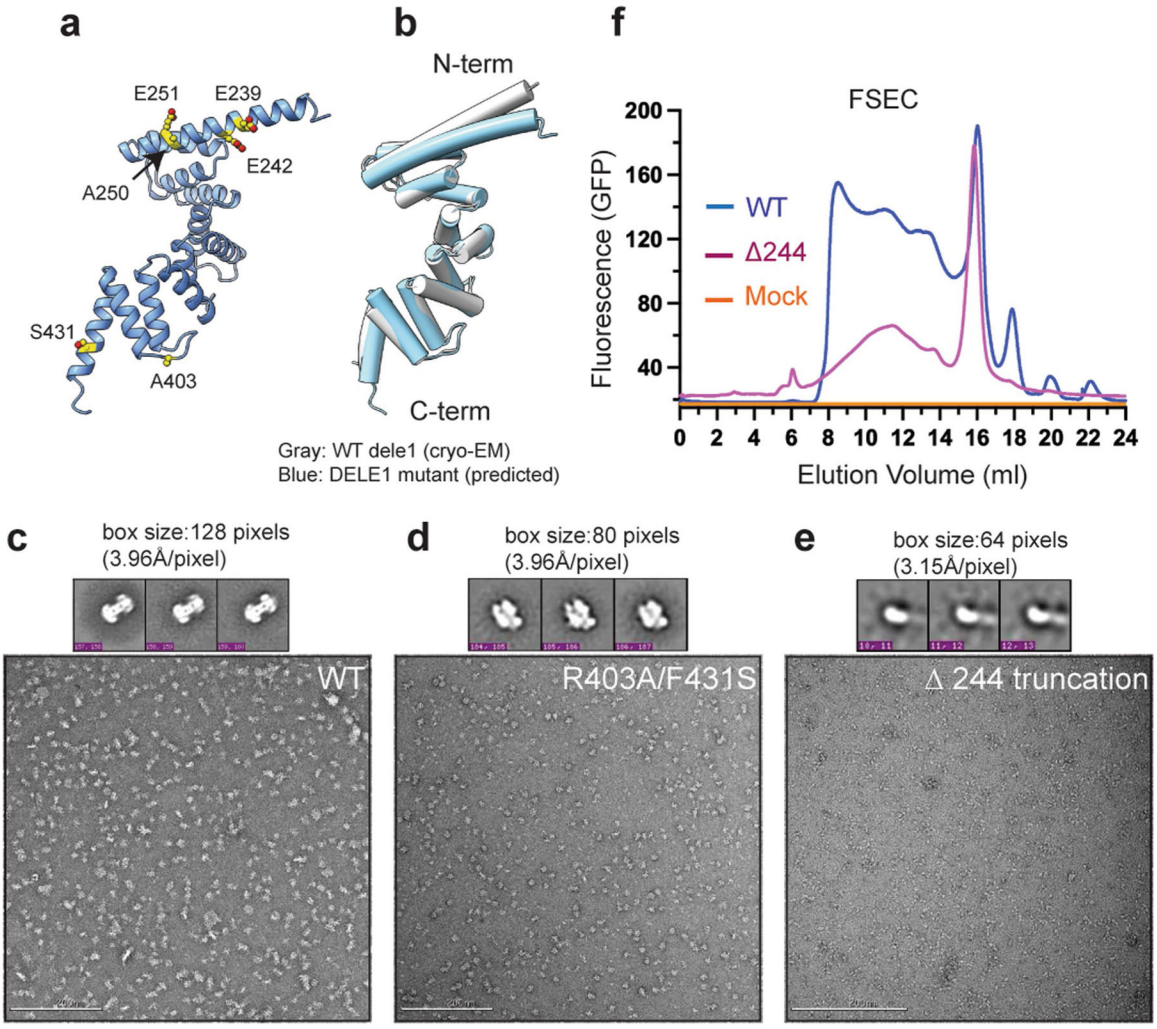

Extended Data Fig. 4 |. AlphaFold2-predicted models of DELE1 and negative stain EM.

a, The AlphaFold2 predicted structure with the DELE1 CTD sequence harboring L239E, L242E, F250A, L251E, R403A, and F431S mutations. The mutated residues are denoted as yellow spheres. **b**, Structural alignment of the DELE1 cryo-EM structure and AlphaFold2-predicted monomeric structure in **a**, showing that the overall predicted structure of the mutant DELE1 is highly similar to the WT DELE1. **c-e**, Representative negative stain EM images of the WT DELE1, the Interface II mutant (R403A/F431S), and the Interface I truncation (Δ244). A total of 326, 257, and 392 images were collected, respectively. **f**, Fluorescence-detection size-exclusion chromatography (FSEC) analysis for WT DELE1^{CTD}-GFP (labeled as WT in blue) and DELE1^{CTD}-GFP Δ244 truncation (labeled as Δ244 in magenta) expressed for 24 hrs post transfection from HEK293T cells.

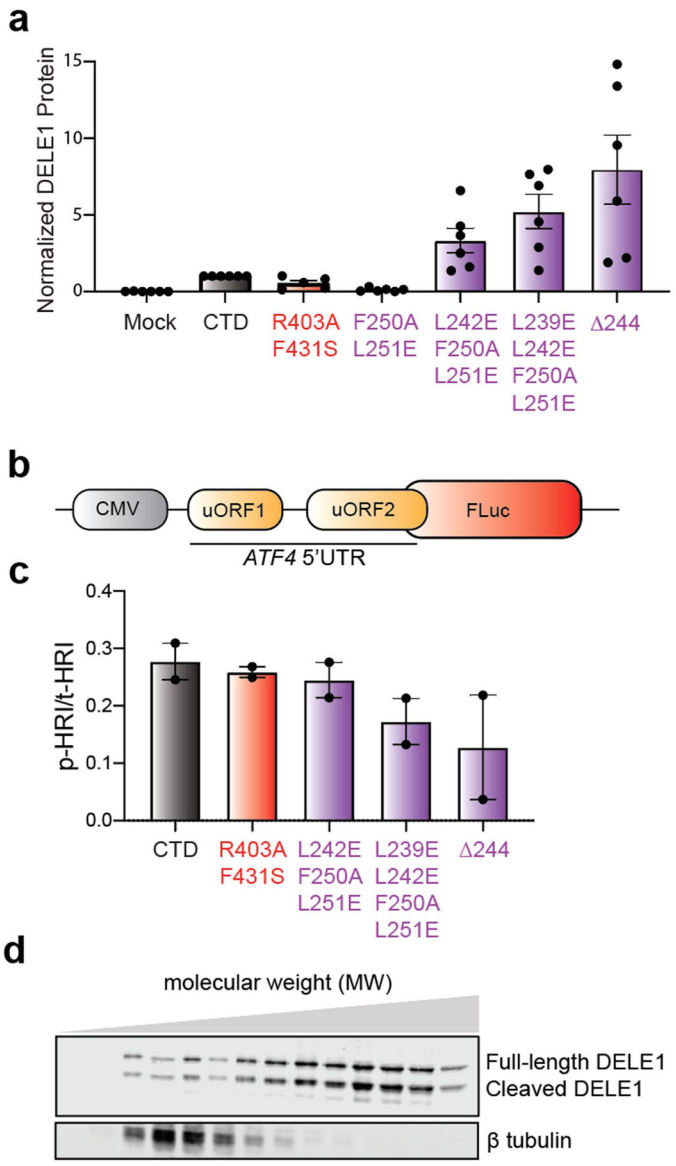

Extended Data Fig. 5 |. Mutant DELE1 expression, ATF4 reporter construct, HRI phosphorylation, and full length DELE1 oligomerization in cells.

a. Quantification of DELE1 mutants expressed in HEK293T cells. (mean ± SEM, n = 6 experimental repeats). One R403A/F431S outlier was excluded using the ROUT outlier test in PRISM. **b**. Description of the ATF4 reporter stable cell line, which contains the upstream open reading frames (uORF1 and uORF2) in the ATF4 5′ untranslated region (*ATF4 5′ UTR*). The ATF4 coding sequence was replaced by a luciferase gene (Fluc). **c**. Quantification of phosphorylated HRI in lysates prepared from HEK293T cells transfected with FLAG-HRI and the different DELE1 mutant constructs show in Fig. 4e. (Error bars show the range, n = 2 experimental repeats). **d**. Immunoblot of the full-length DELE1-mClover protein from sucrose gradient fractions. The 14 sucrose gradient fractions from light to heavy molecular weights (left to right) were blotted with an anti-GFP antibody to detect the DELE1-mClover protein. The upper and lower bands represent the full-length

DELE1 and the cleaved DELE1, respectively. β tubulin was used as a control. Data shown are representative of two independent experiments.

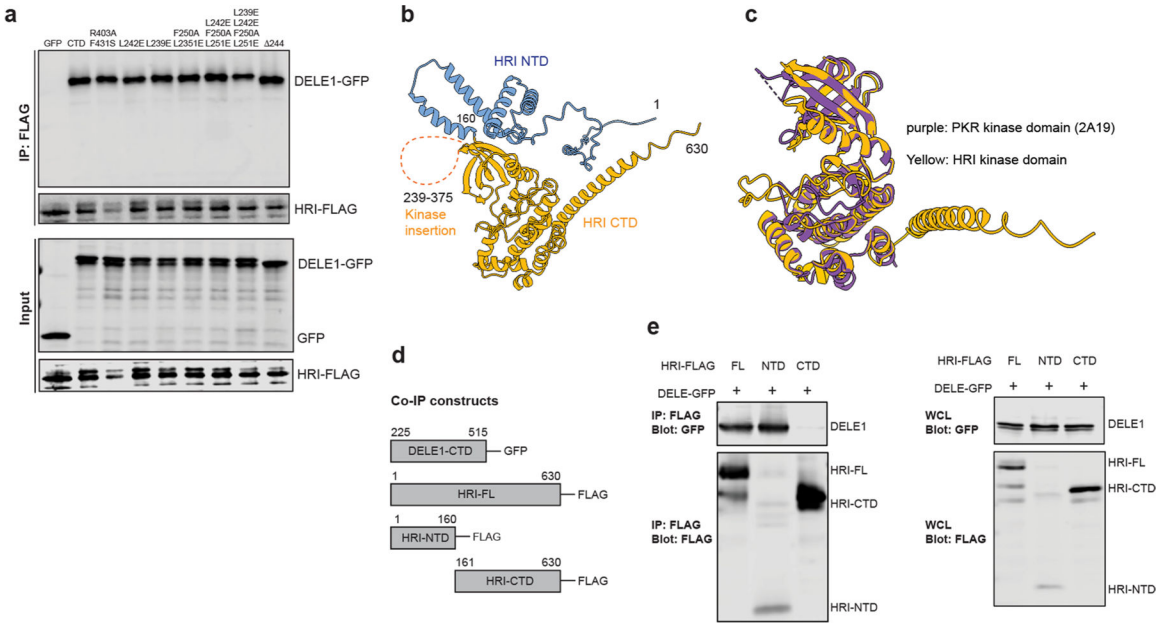

Extended Data Fig. 6 |. HRI NTD mediates its interactions with DELE1.

a. Co-immunoprecipitation of FLAG-tagged HRI and GFP tagged WT DELE1^{CTD} (CTD), and different DELE1 mutants. Anti-GFP antibody and Anti-FLAG antibody were used to detect DELE1 and HRI, respectively. **b**. The AlphaFold2 model of HRI. The HRI N terminal domain (NTD: 1–160) is colored blue, and the HRI C terminal domain (CTD: 161–630) is colored yellow. The disordered kinase insertion region (239–375) from the AlphaFold2 model was deleted and instead shown as dashed line. **c**. Structural alignment for the kinase domains of PKR and HRI. The crystal structure of PKR kinase domain (PDB: 2A19) is colored purple, and the HRI kinase domain is yellow. **d**. Schematic of DELE1 and HRI constructs used for co-immunoprecipitation (co-IP). **e**. Co-IP of GFP-tagged WT DELE1 C-terminal domain (CTD), and different Flag tagged HRI constructs including full-length HRI (FL), HRI N-terminal domain (NTD), and HRI C-terminal domain (CTD). An anti-GFP antibody and anti-FLAG antibody were used to detect DELE1 and HRI, respectively. Left: Immunoblotting of designated proteins from IP fractions. Right: Immunoblotting of designated proteins from whole cell lysis (WCL) fractions. In **6a** and **6e**, Data shown are representative of two independent experiments.

Supplementary Material

Refer to Web version on PubMed Central for supplementary material.

Acknowledgements

We thank B. Anderson at the Scripps Research Electron Microscopy Facility for microscopy support. We thank C. Bowman and J.-C. Ducom at Scripps Research High Performance Computing core for computational support. We thank T. S. Xiao at Case Western Reserve University for kindly sharing the MBP-tagged vectors. We thank B. Basanta for his valuable comments on designing DELE1 mutants. This work is supported by the National

Institutes of Health (NIH) (NS125674 to R.L.W. and NS095892 to R.L.W. and G.C.L). A.S.S. is supported by the NIH F31AG071162 and the Olson-King Endowed Skaggs Fellowship from Scripps Research. Cryo-EM data were acquired using shared instrumentation funded by NIH S10OD032467 to G.C.L. Computational analyses of EM data were performed using shared instrumentation funded by NIH S10OD021634 to G.C.L.

Data availability

The cryo-EM reconstruction and associated atomic model of DELE1^{CTD} have been deposited to the Electron Microscopy Data Bank and PDB under accession numbers EMDB EMD-27269 and PDB 8D9X, respectively. All data needed to evaluate the conclusions in the paper are present in the paper and the supporting information. All the plasmids used in this study are available from the corresponding authors upon reasonable request. Source data are provided with this paper.

References

1. Palikaras K, Lionaki E & Tavernarakis N Mechanisms of mitophagy in cellular homeostasis, physiology and pathology. Nat. Cell Biol 20, 1013–1022 (2018). [PubMed: 30154567]
2. Spinelli JB & Haigis MC The multifaceted contributions of mitochondria to cellular metabolism. Nat. Cell Biol 20, 745–754 (2018). [PubMed: 29950572]
3. Lee SS et al. A systematic RNAi screen identifies a critical role for mitochondria in C. elegans longevity. Nat. Genet 33, 40–48 (2003). [PubMed: 12447374]
4. Moehle EA, Shen K & Dillin A Mitochondrial proteostasis in the context of cellular and organismal health and aging. J. Biol. Chem 294, 5396–5407 (2019). [PubMed: 29622680]
5. Pakos-Zebrucka K et al. The integrated stress response. EMBO Rep 17, 1374–1395 (2016). [PubMed: 27629041]
6. Guo X et al. Mitochondrial stress is relayed to the cytosol by an OMA1–DELE1–HRI pathway. Nature 579, 427–432 (2020). [PubMed: 32132707]
7. Fessler E et al. A pathway coordinated by DELE1 relays mitochondrial stress to the cytosol. Nature 579, 433–437 (2020). [PubMed: 32132706]
8. Ahola S et al. OMA1-mediated integrated stress response protects against ferroptosis in mitochondrial cardiomyopathy. Cell Metab 34, 1875–1891 (2022). [PubMed: 36113464]
9. Fessler E, Krumwiede L & Jae LT DELE1 tracks perturbed protein import and processing in human mitochondria. Nat. Commun 13, 1853 (2022). [PubMed: 35388015]
10. Jin T et al. Design of an expression system to enhance MBP-mediated crystallization. Sci. Rep 7, 40991 (2017). [PubMed: 28112203]
11. Krissinel E & Henrick K Inference of macromolecular assemblies from crystalline state. J. Mol. Biol 372, 774–797 (2007). [PubMed: 17681537]
12. Chen T et al. Chemical genetics identify eIF2α kinase heme-regulated inhibitor as an anticancer target. Nat. Chem. Biol 7, 610–616 (2011). [PubMed: 21765405]
13. Sekine Y et al. A mitochondrial iron-responsive pathway regulated by DELE1. Mol. Cell 83, 2059–2076.e6 (2023). [PubMed: 37327776]
14. Suomalainen A & Battersby BJ Mitochondrial diseases: the contribution of organelle stress responses to pathology. Nat. Rev. Mol. Cell Biol 19, 77–92 (2018). [PubMed: 28792006]
15. Sun N, Youle RJ & Finkel T The mitochondrial basis of aging. Mol. Cell 61, 654–666 (2016). [PubMed: 26942670]
16. Shpilka T & Haynes CM The mitochondrial UPR: mechanisms, physiological functions and implications in ageing. Nat. Rev. Mol. Cell Biol 19, 109–120 (2018). [PubMed: 29165426]
17. Costa-Mattioli M & Walter P The integrated stress response: from mechanism to disease. Science 368, eaat5314 (2020). [PubMed: 32327570]
18. Dar AC, Dever TE & Sicheri F Higher-order substrate recognition of eIF2α by the RNA-dependent protein kinase PKR. Cell 122, 887–900 (2005). [PubMed: 16179258]

19. Dey M et al. Mechanistic link between PKR dimerization, autophosphorylation, and eIF2α substrate recognition. Cell 122, 901–913 (2005). [PubMed: 16179259]
20. Zappa F et al. Signaling by the integrated stress response kinase PKR is fine-tuned by dynamic clustering. J. Cell Biol 221, e202111100 (2022). [PubMed: 35522180]
21. Mattson MP, Gleichmann M & Cheng A Mitochondria in neuroplasticity and neurological disorders. Neuron 60, 748–766 (2008). [PubMed: 19081372]
22. Prisant MG, Williams CJ, Chen VB, Richardson JS & Richardson DC New tools in MolProbity validation: CaBLAM for CryoEM backbone, UnDowser to rethink “waters”, and NGL Viewer to recapture online 3D graphics. Protein Sci 29, 315–329 (2019). [PubMed: 31724275]
23. Herzik MA Jr. Setting up parallel illumination on the Talos Arctica for high-resolution data collection. Methods Mol. Biol 2215, 125–144 (2021). [PubMed: 33368002]
24. Herzik MA Jr., Wu M & Lander GC Achieving better-than-3-resolution by single-particle cryo-EM at 200 keV. Nat. Methods 14, 1075–1078 (2017). [PubMed: 28991891]
25. Suloway C et al. Automated molecular microscopy: the new Leginon system. J. Struct. Biol 151, 41–60 (2005). [PubMed: 15890530]
26. Lander GC et al. Appion: an integrated, database-driven pipeline to facilitate EM image processing. J. Struct. Biol 166, 95–102 (2009). [PubMed: 19263523]
27. Zheng SQ et al. MotionCor2: anisotropic correction of beam-induced motion for improved cryo-electron microscopy. Nat. Methods 14, 331–332 (2017). [PubMed: 28250466]
28. Punjani A, Rubinstein JL, Fleet DJ & Brubaker MA cryoSPARC: algorithms for rapid unsupervised cryo-EM structure determination. Nat. Methods 14, 290–296 (2017). [PubMed: 28165473]
29. Tan YZ et al. Addressing preferred specimen orientation in single-particle cryo-EM through tilting. Nat. Methods 14, 793–796 (2017). [PubMed: 28671674]
30. Adams PD et al. PHENIX: a comprehensive Python-based system for macromolecular structure solution. Acta Crystallogr. D 66, 213–221 (2010). [PubMed: 20124702]
31. Emsley P, Lohkamp B, Scott WG & Cowtan K Features and development of Coot. Acta Crystallogr. D 66, 486–501 (2010). [PubMed: 20383002]
32. Pettersen EF et al. UCSF Chimera-a visualization system for exploratory research and analysis. J. Comput. Chem 25, 1605–1612 (2004). [PubMed: 15264254]
33. Pettersen EF et al. UCSF ChimeraX: structure visualization for researchers, educators, and developers. Protein Sci 30, 70–82 (2021). [PubMed: 32881101]

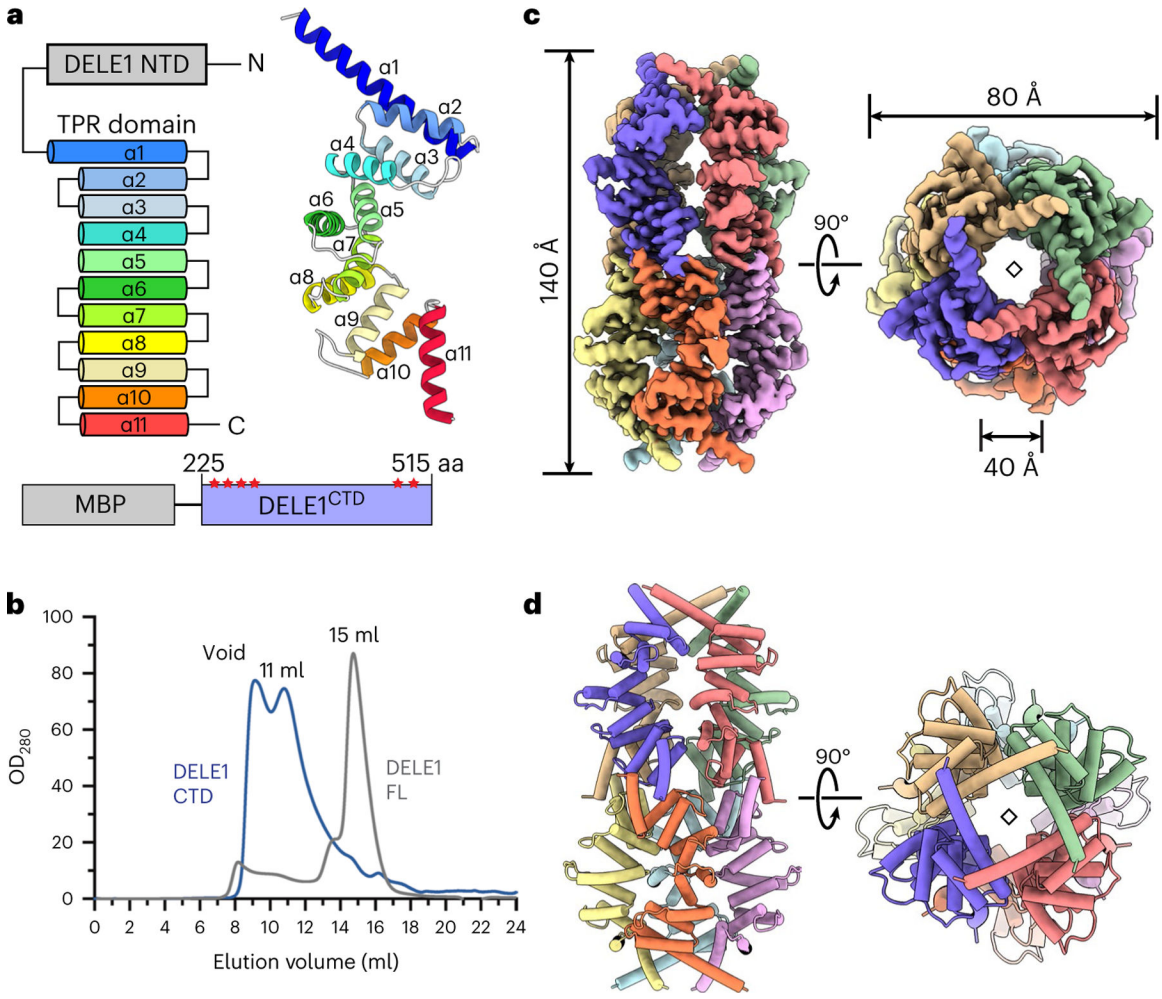

Fig. 1 |. Cryo-EM structure of the oligomeric DELE1^{CTD}.

a, Left: domain organization of the DELE1 protein, with the TPR helices individually colored. Right: a protomer from our cryo-EM structure, with the helices of the TPR domain colored as in the diagram. Bottom: a schematic of the MBP-tagged construct used for producing the DELE1 samples in this study. Amino acids (aa) 225–515 are designated as the DELE1 C-terminal domain (DELE1^{CTD}). The approximate location of each substitution (p.L239E, p.L242E, p.F250A, p.L251E, p.R403A, and p.F431S) introduced into DELE1 for biochemical and cellular analysis (Figs. 3 and 4) is designated with a red star. **b**, Size-exclusion chromatograms of purified recombinant MBP-tagged full-length DELE1 (gray) and DELE1^{CTD} (blue), which eluted at peak volumes of 15 and 11 ml, respectively. OD_{280}, optical density at 280 nm. **c**, Orthogonal views of the cryo-EM reconstruction of the D_4-symmetric DELE1^{CTD} oligomer. Each subunit is shown in a different color. **d**, The DELE1^{CTD} atomic model is shown using the same orientations and subunit coloring as in **c**.

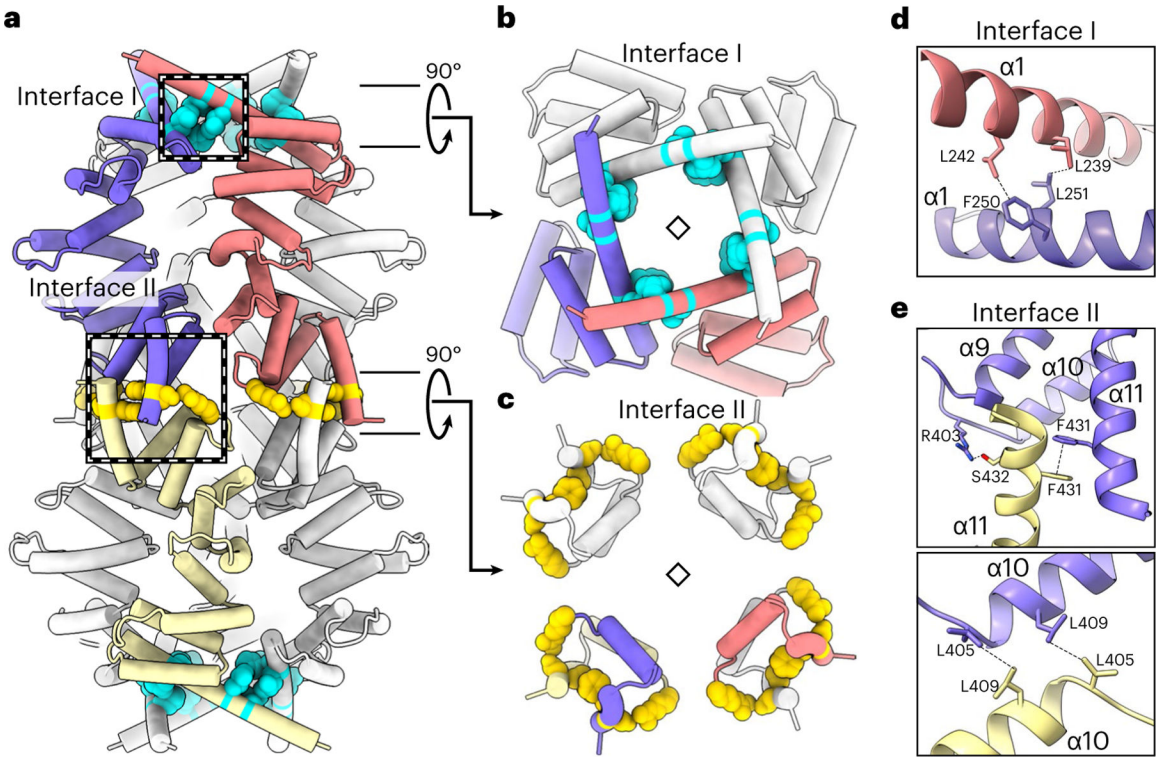

Fig. 2 |. Two interfaces contribute to DELE1^{CTD} oligomerization.

a, A cartoon representation of the DELE1^{CTD} octamer, with three subunits highlighted to show the two distinct interaction interfaces, and residues involved in the interactions represented as spheres (cyan at interface I, gold at interface II). The purple subunit interacts with the red subunit at the N-terminal α1-helix crown, and with the yellow subunit at the C terminus of the TPR. **b**, An axial view of the DELE1^{CTD} crown, demonstrating how the inter-subunit interactions (cyan) link the four subunits together in a fourfold symmetric arrangement. **c**, The axial view of a central cross-section of the DELE1^{CTD} octamer shows that the inter-subunit interactions (gold) establish dimeric assemblies. **d**, A close-up view of the inter-protomer interactions at interface I, enclosed by the top dashed box in **a**. Residues F250 and L251 in the α1-helix from the purple-colored subunit interact with L239 and L242 in the α1-helix of the neighboring red subunit. Hydrophobic interactions between F250 and L242 and between L251 and L239 are represented as dashed lines. **e**, Top: close-up views of the subunit C-terminal TPR interface (interface II), with interacting residues shown as sticks. R403 from the loop preceding the α10-helix of the purple subunit hydrogen bonds with S432 in the α11-helix of the yellow subunit. Symmetrically related F431 residues from neighboring subunits are positioned for π-stacking interaction. Bottom: a close-up view of the inter-protomer interface visualized from the lumen, depicting the C_2-symmetric interactions between L405 and L409 of the adjacent subunits.

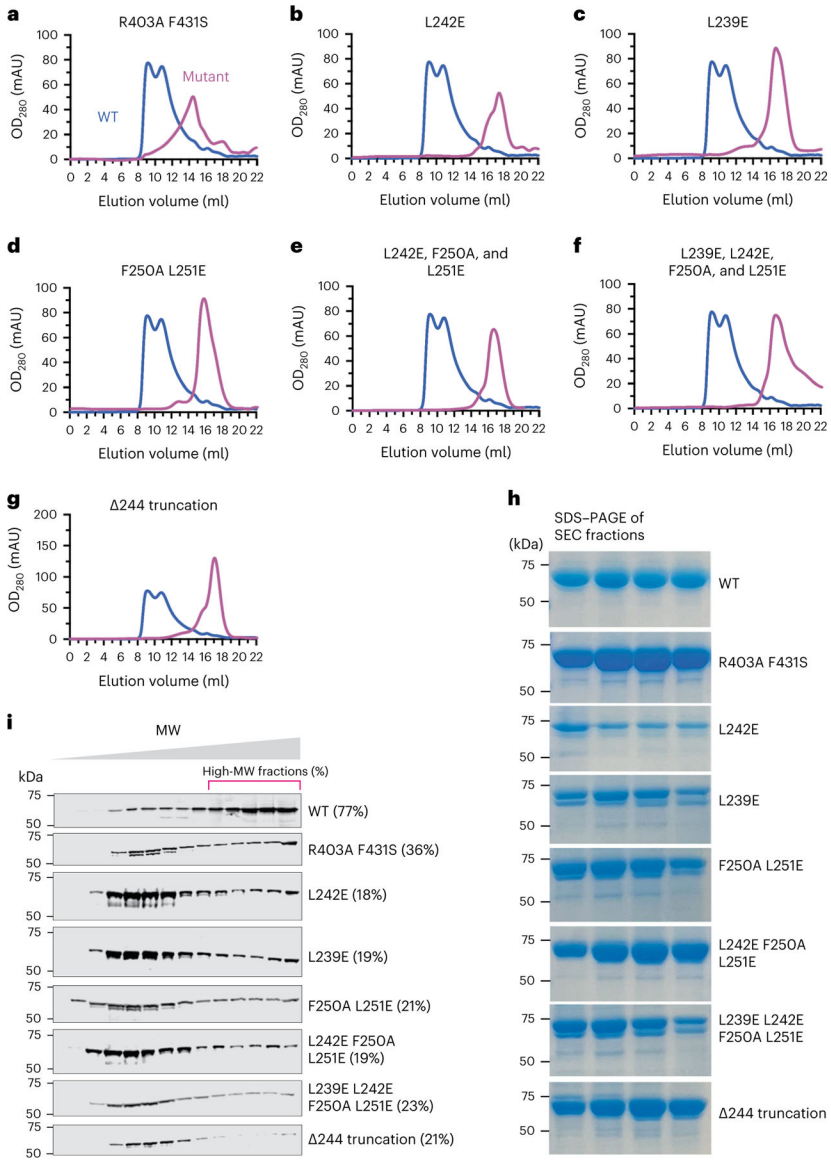

Fig. 3 |. Structure-guided substitutions disrupt DELE1^{CTD} oligomer formation.

a, Size-exclusion chromatograms of the WT DELE1^{CTD} and the interface II mutant (labeled as R403A F431S), colored blue and magenta, respectively. **b**–**g**, Size-exclusion chromatograms of WT DELE1^{CTD} overlaid with different interface I substitutions, including p.L242E (**b**), p.L239E (**c**), p.F250A and p.L251E (**d**), p.L242E, p.F250A, and p.L251E (**e**), p.L239E, p.L242E, p.F250A, and p.L251E (**f**), and the Δ244 truncation (**g**). **h**, SDS–PAGE gels for the peak fractions of the WT and the various DELE1^{CTD} mutants. Data shown are representative of two independent experiments. **i**, Immunoblot of WT and mutant DELE1^{CTD} proteins from sucrose gradient fractions. The 14 sucrose gradient fractions from light to heavy molecular weights (left to right) were blotted with an anti-GFP antibody to detect the DELE1^{CTD}-GFP fusion proteins. The percentages of the last five fractions were quantified and calculated against the total protein level in all fractions. MW, molecular weight. Data shown are representative of two independent experiments.

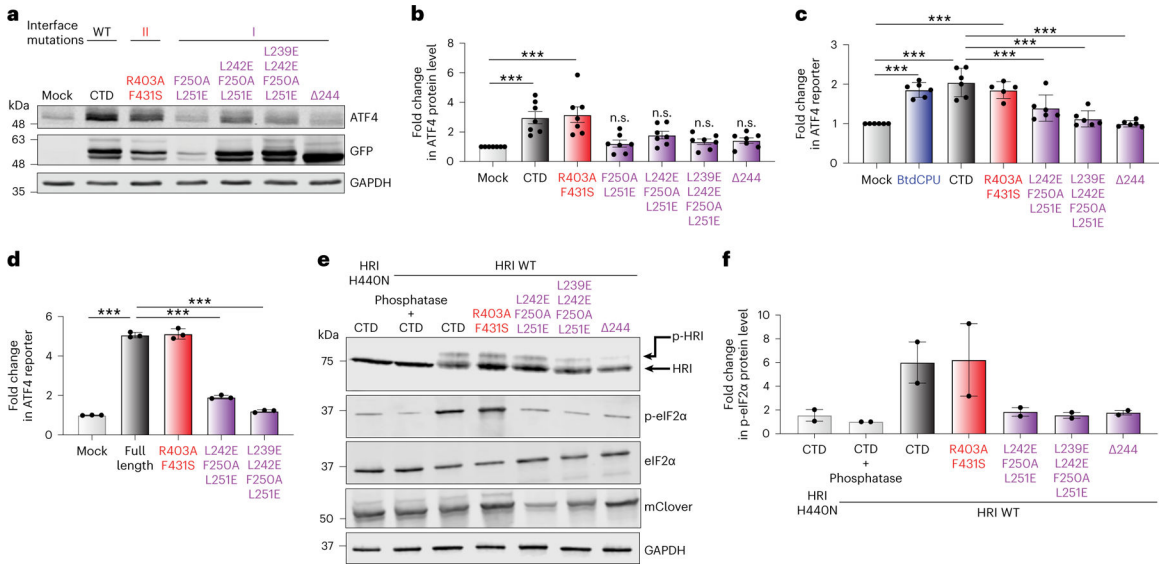

Fig. 4 |. Disruption of DELE1 interface I interactions compromises HRI activity.

All substitutions are colored according to the DELE1 interface (purple for Interface I, red for Interface II). **a**, An immunoblot of ATF4 in lysates prepared 24 h post-transfection with WT DELE1^{CTD} (labeled as CTD), DELE1^{CTD}-R403A F431S, DELE1^{CTD}-F250A L251E, DELE1^{CTD}-L242E F250A L251E, DELE1^{CTD}-L239E L242E. F250A L251E, or the Δ244 truncation. **b**, Quantification of ATF4 in immunoblots shown in **a**. Mean ± s.e.m., $n = 7$ experimental replicates. ***$P < 0.005$, one-way analysis of variance (ANOVA) relative to mock transfected cells. n.s., not significant. **c**, ATF4 activation measured by luciferase in HEK293T cells stably expressing the ATF4-FLuc ISR reporter (Extended Data Fig. 5b) transfected with empty vector, WT DELE1^{CTD} (labeled as CTD), or the mutants described in **a** (mean ± s.e.m., $n = 6$ experimental repeats). Cells treated with the HRI activator BtdCPU (10 μM, 6 h) are shown as a control. ***$P < 0.005$, one-way ANOVA. One DELE1^{CTD}-R403A F431S outlier was excluded using the ROUT outlier test in PRISM. **d**, ATF4 activation measured in HEK293T cells that were depleted of *DELE1* using CRISPR interference and that expressed the ATF4-mApple reporter[6]. Cells were transfected with full-length WT DELE1, full-length DELE1 containing the interface II p.R403A and p.F431S substitutions, full-length DELE1 containing the interface I p.L242E, p.F250A, and p.L251E substitutions, or full-length DELE1 containing the interface I p.L239E, p.L242E, p.F250A, and p.L251E substitutions. The ATF4 reporter level was measured 16 h post-transfection using flow cytometry. Mean ± s.e.m., $n = 3$ experimental replicates. ***$P < 0.005$ for one-way ANOVA. **e**, WT FLAG-HRI was co-expressed with WT DELE1^{CTD} (labeled as CTD) or the mutants in **a**. An HRI-kinase-dead mutant (p.H440N) and phosphatase-treated lysis were used as controls. Immunoblots are shown for phosphorylated HRI (p-HRI) and phosphorylated eIF2α (p-eIF2α) at 8 h post-transfection. **f**, Quantification of p-eIF2α in the immunoblots in **e**. Error bars show the range, $n = 2$ experimental replicates.

Table 1 |

Cryo-EM data collection, refinement, and validation

	EMD-27269 PDB 8D9X
Data collection	
Microscope	Talos Arctica
Voltage (keV)	200
Detector	K2 Summit (Counting)
Magnification (nominal/calibrated)	×36,000/×43,478
Exposure navigation	Image shift to 16 holes
Data acquisition software	Leginon
Total electron exposure (e^{-}/Å^2)	50
Exposure rate (e^{-}/pixel/sec)	6.75
Frame length (ms)	200
Number of frames per micrograph	49
Pixel size (Å)	1.15
Defocus range (μm)	−0.7 to −1.2
Micrographs collected (no.)	13,164
Reconstruction	
Image processing package	cryoSPARC
Total extracted particles (no.)	1,060,000
Refined particles (no.)	92,455
Final particles (no.)	67,067
Symmetry imposed	D_4
Resolution (Å)	
FSC 0.5 (unmasked masked)	4.5/4.0
FSC 0.143 (unmasked/masked)	4.03/3.8
Resolution range (local)	3.3–4.5
3DFSC sphericity	0.9 of 1
Sharpening B-factor (Å^2)	−171.6
Model composition	
Protein residues	1,680
Ligands	0
Model refinement	
Refinement package	Phenix
CC (volume/mask)	0.71/0.71
R.m.s. deviations	
Bond lengths	0.003
Bond angles (°)	0.678
Validation	

	EMD-27269 PDB 8D9X
Map-to-model FSC 0.5	4.1
Ramachandran (%)	
Outliers	0
Allowed	3.19
Favored	96.81
MolProbity score	1.79
Poor rotamers (%)	0.00
Clashscore (all atoms)	11.98
C-beta deviations	0.00
CaBLAM Outliers (%)[22]	0.49
EMRinger score	1.56